Haoyu Ding
Department of Architecture and Civil Engineering,
University of Bath,
Bath BA2 7AY, UK
e-mail: hd484@bath.ac.uk

Guangwei Zhao
Kelvin Hydrodynamics Laboratory,
University of Strathclyde,
Glasgow G20 0TL, UK
e-mail: guangwei.zhao@strath.ac.uk

Tianning Tang
Department of Engineering Science,
University of Oxford,
Oxford OX1 3PJ, UK
e-mail: tianning.tang@eng.ox.ac.uk

Paul H. Taylor
Oceans Graduate School,
The University of Western Australia,
Perth, WA 6009, Australia
e-mail: paul.taylor@uwa.edu.au

Thomas A. A. Adcock
Department of Engineering Science,
University of Oxford,
Oxford OX1 2DL, UK
e-mail: thomas.adcock@eng.ox.ac.uk

Saishuai Dai
Naval Architecture, Ocean and Marine
Engineering Department,
University of Strathclyde,
Glasgow G1 1XQ, UK
e-mail: saishuai.dai@strath.ac.uk

Dezhi Ning
State Key Laboratory of Coastal and Offshore
Engineering,
Dalian University of Technology,
Dalian, Liaoning 116024, China
e-mail: dzning@dlut.edu.cn

Lifen Chen
State Key Laboratory of Coastal and Offshore
Engineering,
Dalian University of Technology,
Dalian 8221, China
e-mail: lifen_chen@dlut.edu.cn

Experimental Investigation of Nonlinear Forces on a Monopile Offshore Wind Turbine Foundation Under Directionally Spread Waves

Accurate prediction of nonlinear wave loading is crucial for designing marine and offshore structures, yet it remains a challenging task. Prior research has primarily focused on unidirectional extreme sea states, revealing that linear loading cannot accurately represent the total wave forces acting on offshore wind turbine foundations, with significant contributions from high-order harmonics. This study broadens the scope to include multidirectional and bidirectional wave interactions with monopile offshore wind turbine foundations. We use a phase-based harmonic separation method to isolate harmonic components in the presence of complex wave scenarios. This approach allows for the clear delineation of individual harmonics from the total wave force by controlling the phase of incident-focused waves. Remarkably, this method is effective even with multidirectional and bidirectional spreading. The clean separation of individual harmonics enables the estimation of contributions from each harmonic. Our findings are in line with previous research, showing that nonlinear loading can constitute up to 40% of the total under certain wave conditions. We have also observed that wider wave spreading reduces nonlinear high-order harmonics, and unidirectional waves induce the most severe nonlinear forces. These insights emphasize the importance of accounting for high-order nonlinear wave loading in offshore structure design. [DOI: 10.1115/1.4067116]

Keywords: wave loads, offshore wind turbine, wave–structure interaction, nonlinear waves, fluid–structure interaction, hydrodynamics, wave mechanics and wave effects

Jinxuan Li
State Key Laboratory of Coastal and Offshore
Engineering,
Dalian University of Technology,
Dalian 116024, China
e-mail: lijx@dlut.edu.cn

Rongquan Wang
State Key Laboratory of Coastal and Offshore
Engineering,
Dalian University of Technology,
Dalian 116024, China
e-mail: rqwang@dlut.edu.cn

Jun Zang[1]
Department of Architecture and Civil Engineering,
University of Bath,
Bath BA2 7AY, UK
e-mail: jz235@bath.ac.uk

1 Introduction

Offshore wind turbines are consistently subjected to harsh environmental loads, which frequently drive their design. Extreme wave loads are found to be broken down into a fundamental component near the incident wave spectral peak frequency, as well as higher harmonics. These higher harmonics arise due to the nonlinearity present in both the incident waves and their interactions with the structure, occurring at frequencies close to integer multiples of the fundamental frequency [1]. The physics and statistics underlying wave–structure interactions present a complex challenge, especially in understanding these strongly nonlinear loads experienced under severe conditions.

A variety of theoretical approaches have been developed to understand wave interactions with cylinders and to quantify the associated higher harmonic loads. Wave diffraction theory, based on classical perturbation expansions up to the second order in wave steepness, has been elaborated by numerous authors [2–4]. Building upon this, the "FNV" model—named after its authors— was established to estimate third-order wave forces on slender cylinders in deep water under the assumption that the incident wave amplitude is comparable to the cylinder radius [5]. This model has generally shown good agreement with experimental results within its range of applicability, as demonstrated by studies such as Refs. [1,6]. Moreover, various researchers have conducted experimental investigations into the higher harmonics of wave loading, including Refs. [6–9]. In addition, Chen et al. [1] have found through experimental research that the nonlinear interaction between waves and a vertical cylinder can generate higher-order harmonic forces, which significantly contribute to the total force magnitude in steep, yet realistic sea states, potentially adding up to an additional 60% to the peak load.

The study by Chen et al. [1] primarily focused on unidirectional waves, and Mj et al. [10] extended it to include an additional type of directionally spread waves. This research is a continuation of these efforts, aiming to further explore higher-order harmonic forces under various wave-spreading conditions. This article emphasizes the experimental design, wave generation, and measurement setup, showing the variety of wave patterns explored and demonstrating the reasonableness and reliability of our novel experiments. We employed the four-phase inversion method, previously shown effective in separating individual harmonics from total wave forces in time histories for unidirectional waves [11], and applied it to various wave spreading conditions. Through this approach, the contribution of each high-order harmonic is investigated. We compare the results across different wave-spreading scenarios in parallel, aiming to illuminate the importance of nonlinearity in these diverse wave conditions.

2 Experiments

The experiments were conducted in the multifunctional tank of the State Key Laboratory of Coastal and Offshore Engineering at Dalian University of Technology. This tank measures 54 m in length and 34 m in width and has a depth of 1.3 m, with an effective area of 45 m long and 28 m wide. The maximum effective water depth is 0.7 m. At one end of the tank, a multidirectional irregular wave maker, developed by the laboratory, is installed. This wave maker consists of 70 wave paddles, each measuring 0.4 m in width and 1.0 m in height. Controlled by a microcomputer, the wave maker ensures high repeatability in wave generation. To minimize wave reflection, energy dissipation devices are installed along the other sides of the tank.

2.1 Metocean Data. The distribution of hourly sea-state parameters for all 36 UK offshore wind farm locations was presented in Ref. [12]. A correlation was found between the radius of the monopile offshore wind turbine foundation and the relative water depth, indicating that larger cylinder radii are expected in deeper water areas. The majority of wind farms satisfy the condition that the water depth does not exceed nine times the cylinder radius among all the 36 UK offshore wind farms. Considering both the sea-state parameters and the operational conditions of the experimental wave tank, we selected two water depths for the experiments: 0.5 m and 0.7 m, the latter being the maximum effective water depth in the tank. Correspondingly, the cylinder model radius was set at 0.125 m. It is important to note that this selection was guided by the operational conditions, rather than by a specific scale ratio. Thus, the ratio of water depth to cylinder radius was used as normalized data in our experimental setup.

In defining the wave conditions for the experiments, realistic environmental data were taken into account during the preliminary design phase. These data provide insights into typical sea states representative of the ocean environments where offshore wind turbines are currently, and will likely be, installed in the near future. To ensure relevance and applicability, the design of new experiments
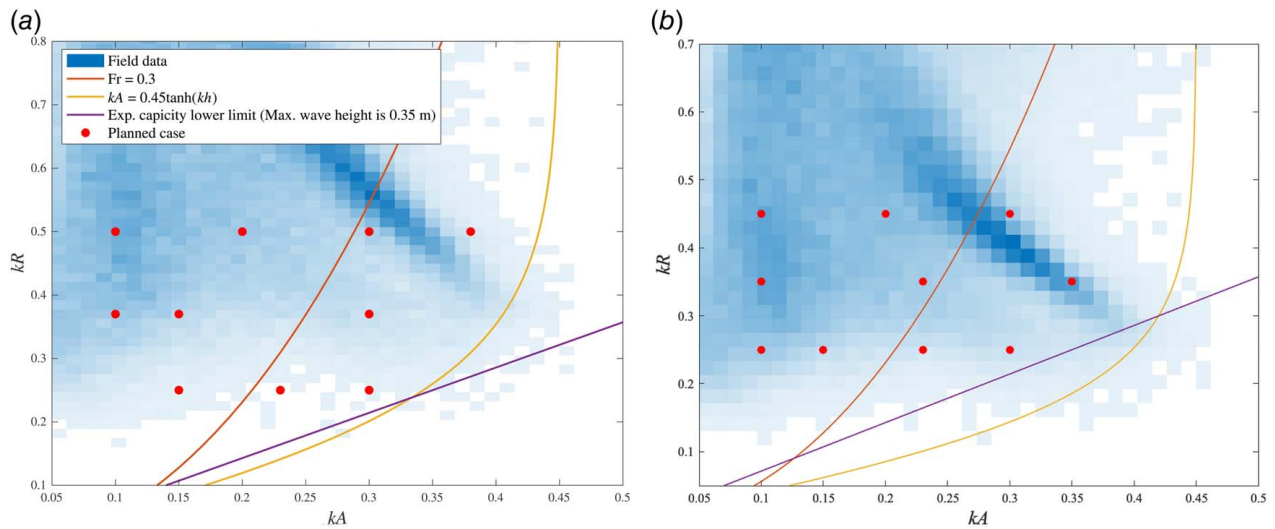
Fig. 1 Experimental test cases in metocean data bin scatters. The data are charted using the wave number-radius ratio (kR) on the y-axis and the wave number-amplitude ratio (kA) on the x-axis. Here, k represents the wave number, R is the radius of the monopile wind turbine foundation, and A denotes the wave amplitude. (a) Water depth of 0.5 m and (b) water depth of 0.7 m.

should be closely aligned with the metocean data, thereby avoiding scenarios that are unlikely to occur in realistic sea states.

In this research, the metocean data were sourced from the ERA 5 dataset provided by the ECMWF, as detailed in Ref. [13]. Figure 1 presents the field data, which encompasses the metocean data from locations in seven countries (the United Kingdom, the United States, China, Australia, France, Germany, and Denmark), spanning from 1940 to 2021. These locations were specifically chosen based on the sites of existing and prospective wind farms in these countries. The ocean wave data has a resolution of 0.5 deg by 0.5 deg, and for our analysis, the nearest node to each wind farm location was selected. Prior rigorous data quality control and validation procedures for this dataset are documented in Ref. [13]. In Fig. 1, three metocean parameters are considered: the maximum individual wave height, the wave period corresponding to the maximum individual wave height, and the averaged local water depth. The wave amplitude, denoted as A in the figure, is defined as half of the maximum individual wave height. The wave number, k, is determined using the finite depth dispersion relationship with the averaged local water depth and the wave period corresponding to the maximum individual wave height. The cylinder radius, R, is based on the same water depth to cylinder radius ratio used in our experimental design. This ratio is 4 in Fig. 1(a) and 5.6 in Fig. 1(b).

Three reference lines in Fig. 1 also aid in defining the test wave conditions. The orange line represents a Froude number (Fr) of 0.3, which, as found in Ref. [8], is a good predictor of a secondary load cycle. This phenomenon, significant in severe wave conditions, greatly impacts cylinder "ringing" response. We use Fr = 0.3 to indicate the potential for secondary load cycle occurrence. The yellow line, defined by $kA = 0.45 \tanh(kd)$ where d is the water depth, follows the criteria used in Ref. [14] for demarcating the limit of breaking waves. The purple line signifies the limit of the wave tank capacity. Due to the limitations of the wave paddles, a maximum wave height of 0.35 m is considered.

Guided by the aforementioned references, the test wave conditions planned for this study are designed to encompass a broad spectrum of wave regimes. These range from gentle waves to more severe conditions, including those with secondary load cycles or near-breaking waves. The selected conditions are representative of realistic sea states that are typically encountered by wind turbine farms. For each water depth, a total of ten test cases have been chosen to ensure a comprehensive examination of these varied wave environments.
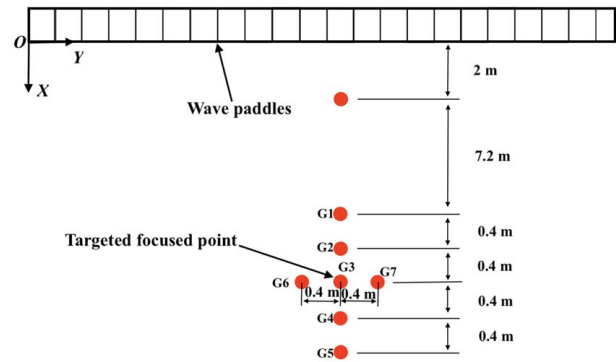
Fig. 2 Wave gauge setup in the empty tank for wave generation

2.2 Wave Generation. In this research, we generate and analyze focused wave groups based on NewWave theory, as described in Refs. [15,16]. These wave groups match the averaged shape of the largest events in the random time series, representing short-term severe wave conditions. The target focus point of these waves is at the center of the cylinder. The wave amplitude planned in Sec. 2.1 refers to the main crest's amplitude at the focus point, while the corresponding wave period (related to the wave number, k, in Fig. 1) is the peak period of the focused wave groups. These waves are generated using the JONSWAP spectrum [17] with a peak enhancement factor of $\gamma = 3.3$. Nonlinear evolution, which is expected in steep wave groups during propagation along the wave tank [18,19], is taken into account. Local properties of the wave group profiles at the focus are measured in the empty tank (i.e., without the cylinder present), and the same groups are used for subsequent tests involving cylinder interaction. Wave gauges, as depicted in Fig. 2, are installed in the empty tank. The target focus point ($G3$), which is also the center of the cylinder, is placed 10 m away from the wave paddles.

In our experiments, various wave-spreading conditions are investigated. In addition to unidirectional waves, the study also examines bidirectional waves, which are characterized by two crossing wave groups with identical wave amplitude and peak wave period intersecting at the focus point. For these bidirectional waves, the angle (θ) between the two groups is set to 20 deg and 40 deg.
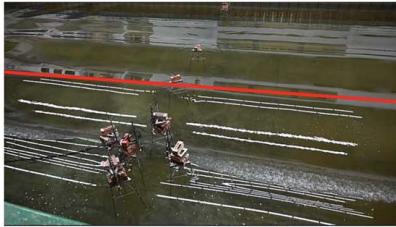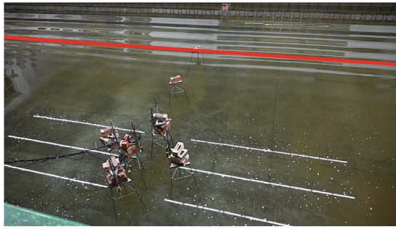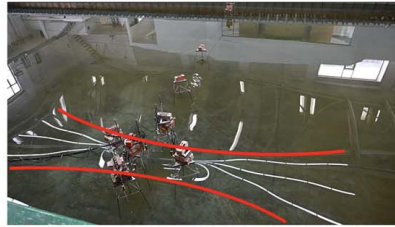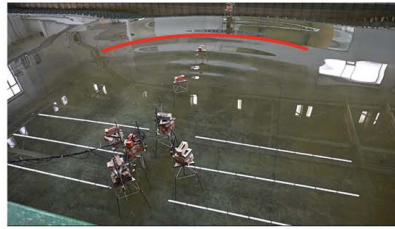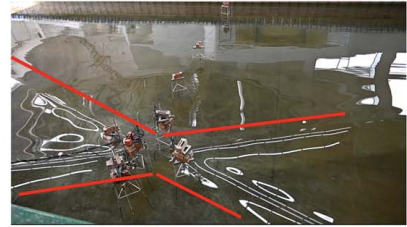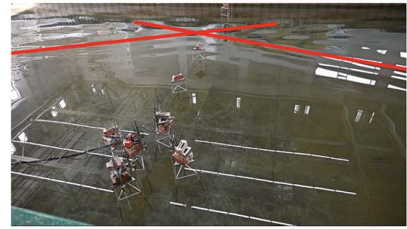
Fig. 3 Wave spreading patterns in the wave tank. The top row shows the initial wave propagation from the wave paddles, while the bottom row captures the waves focusing at the focus point.

Fig. 4 The cylinder installation and force measurements

Furthermore, the multidirectional waves in the experiments are generated using the Mitsuyasu-type spreading function, following the definition by Ref. [20]. For more details, readers are referred to Refs. [21,22]. Regarding the multidirectional waves, the root-mean-square angle (σ) is set to approximately 20 deg and 30 deg, corresponding to spreading factors of 15 and 7, respectively.

To ensure that the various spreading waves accurately converge at the targeted focus point, $G3$, we implemented a series of trial tests with the wave gauges layout depicted in Fig. 2. The coordinates are shown in the figure. We utilized wave gauge pairs ($G1$ and $G5$, $G2$ and $G4$) to confirm wave focusing at $G3$ along the X-axis, according to their symmetric characteristics. After adjusting the focus along the X-axis, we then ensured that the wave profiles at $G6$ and $G7$ were either close to identical or within an acceptable margin of error. This step was crucial to verify that the wave groups also converged accurately at $G3$ along the Y-axis. By employing this method, we ensured that the generated waves were focused at the targeted point under real test conditions.

After completing the calibration for each wave condition, various wave spreading patterns were successfully generated, as illustrated in Fig. 3. In the case of the unidirectional waves, due to the wide dimensions of the wave tank, the influence of the side walls on the waves around the focus point can be completely disregarded. For the multidirectional waves, the wave patterns at the focus point exhibit a hyperbolic shape, while the bidirectional waves form an X-shape at the focus point. Detailed time histories of the wave profiles at the focus point, illustrating the results of the wave generation process, are presented in Sec. 3.1.

2.3 Force and Pressure Measurement. The cylinder is positioned at the wave focus point. As depicted in Fig. 4, the cylinder is rigidly fixed at both the top and bottom. Force measurements are made at the support points at the top and bottom of the cylinder, also illustrated in Fig. 4. To measure point pressure on the cylinder surface, pressure probes are installed according to the layout shown in Fig. 5. Three pressure probes are positioned at the front stagnation points of the cylinder. Positioned 0.1 m beneath the still water level, pressure probes numbered 3–7 are mounted on one side of the cylinder. Pressure probe number 8 is installed opposite probe number 5 to track symmetric characteristics when waves interact with the cylinder. Two identical sets of pressure probes are installed on the cylinder surface, tailored for the two different water depths of 0.5 m and 0.7 m.

To ensure the reliability of the setup and installations used in our experiments for data generation and collection, several repeat tests were conducted throughout the experimental process. To demonstrate the robustness of our experimental setup, even under severe conditions, we selected a representative unidirectional wave test case from the steep wave regime. The results of this test are presented in Figs. 6 and 7, with the test parameters including a main crest wave amplitude of 0.14 m, a peak wave period of 1.64 s, and a water depth of 0.7 m.

Figure 6 illustrates the total force exerted on the cylinder. Notably, a wiggle around 27.5 s marks a secondary load cycle, indicative of severe wave conditions. This feature, along with the crest and trough values of the total force, exhibits a high degree of consistency between the repeat tests, affirming the accurate and realistic reproduction of the data. Additionally, Fig. 7 presents a comparison of point pressure data. Given that total force is derived through integration, and point pressure data are inherently more sensitive, precise replication is crucial. The results from various pressure probes display a good alignment between the repeats, further validating the reliability of our experimental setup.

3 Data Processing

Building on the assumption of a generalized Stokes-type harmonic series [23] in both frequency and wave steepness for the free-surface elevation and horizontal wave loads in focused wave groups, Zang et al. [24] and Chen et al. [1] successfully extracted higher harmonics in their interactions using a two-phase inversion method. This method enabled the separation of odd and even harmonics in time histories. To achieve a more effective separation
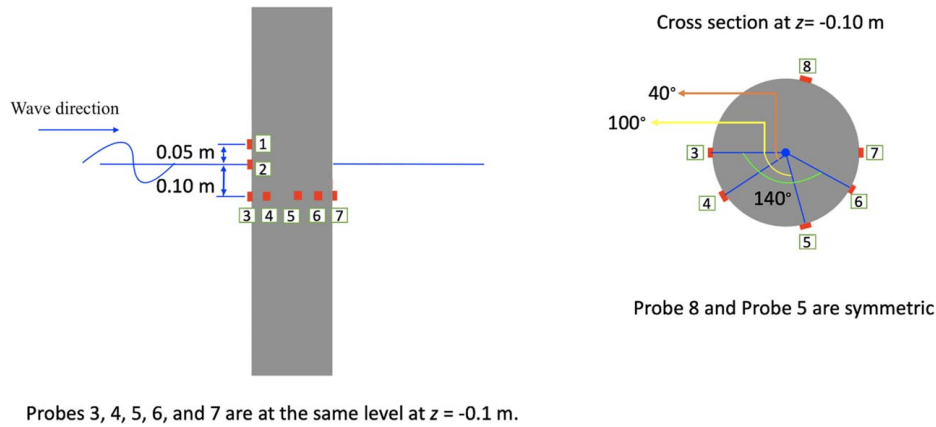
Probes 3, 4, 5, 6, and 7 are at the same level at z = -0.1 m.

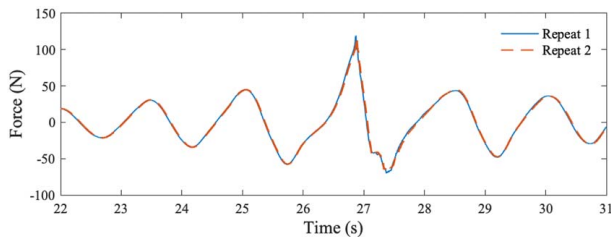**Fig. 5   Setup of point pressure probes around the cylinder**

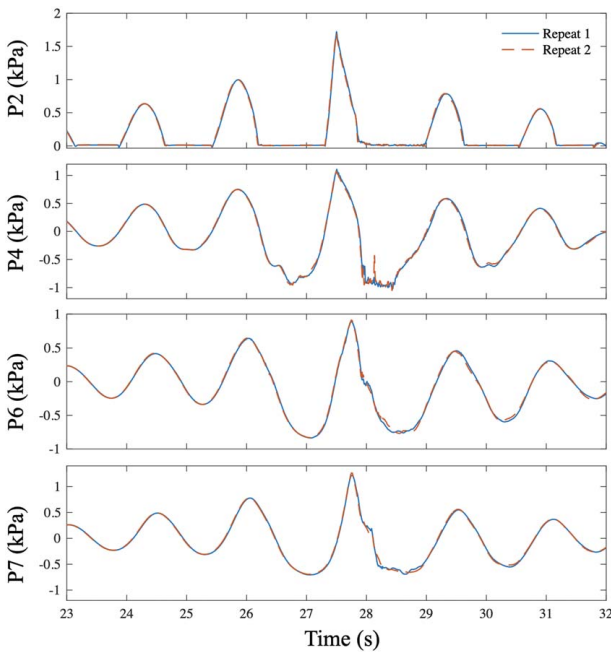**Fig. 6   Two repeats of total wave inline force on cylinder surface**

Fig. 7   Two repeats of point pressure from variously located pressure probes

of harmonics, Fitzgerald et al. [11] developed a four-phase method, generating additional force signals corresponding to further phase shifts of the linear paddle signal. This involves considering four runs for each test case with wave groups generated by the same paddle signal, where the phase of each Fourier component is shifted by 0 deg, 90 deg, 180 deg, and 270 deg. This results in four force time histories: F_0, F_{90}, F_{180}, and F_{270}. Here, we adopt the four-phase method to extract individual high-order harmonic

Stokes-type components. The required linear combinations of these four-phase shifted runs are as follows:

$$\frac{(F_0 - F_{90}^H - F_{180} + F_{270}^H)}{4} = Af_{11}\cos\varphi + A^3 f_{31}\cos\varphi + O(A^5),$$

$$\frac{(F_0 - F_{90} + F_{180} - F_{270})}{4} = A^2 f_{22}\cos 2\varphi + A^4 f_{42}\cos 2\varphi + O(A^6),$$

$$\frac{(F_0 + F_{90}^H - F_{180} - F_{270}^H)}{4} = A^3 f_{33}\cos 3\varphi + O(A^5),$$

$$\frac{(F_0 + F_{90} + F_{180} + F_{270})}{4} = A^2 f_{20} + A^4 f_{44}\cos 4\varphi + O(A^6) \qquad (1)$$

In order, these combinations extract the linear (first harmonic), the second harmonic sum, the third harmonic sum, and finally, the second harmonic difference, and the fourth harmonic sum terms, where the F^H refers to the Hilbert transform of the force time histories. The coefficients f_{mn} conceptually represent wave-to-force transfer functions. The wave-to-force transfer describes how wave properties (such as amplitude and phase) translate into forces acting on a structure, as described in the Stokes-type expansion. Specifically, these functions illustrate how different harmonics of the wave contribute to the overall force. f_{mn} denotes the contribution of the mth-order harmonic of the incident waves to the nth-order harmonic of the wave forces. Additionally, $\varphi = \omega t + \varphi_0$ denotes the phase of the linear component of the incident wave, incorporating a prescribed phase shift φ_0.

3.1 Four-Phase Alignment of Incident Waves. The previous work has demonstrated that effective four-phase aligned unidirectional waves can be generated in experiments [25,26]. This section introduces the four-phase alignment of both multidirectional and unidirectional waves as generated in our experiments. Figure 8(a) displays the bidirectional waves produced in the wave tank at the focus point, characterized by a main crest amplitude of 0.075 m, a peak wave period of 1.51 s, a water depth of 0.7 m, and a 40 deg angle between the two crossing waves. The 0 deg phase waves exhibit a well-focused wave profile, and the time histories show that the 90 deg, 180 deg, and 270 deg phase waves are well aligned with the 0 deg phase waves, exhibiting the correct phase shifting. This precise alignment is crucial for the successful application of the four-phase method in subsequent force harmonic extractions. Similarly, Fig. 8(b) illustrates effective alignment for the multidirectional waves, which feature a main crest amplitude of 0.075 m, a peak wave period of 1.51 s, a water depth of 0.7 m, and a root-mean-square angle of 30 deg corresponding to a spreading factor of 7.

Overall, the results in Fig. 8 have demonstrated the effective application of the four-phase method in experimentally generating both bidirectional and multidirectional waves. The accuracy of
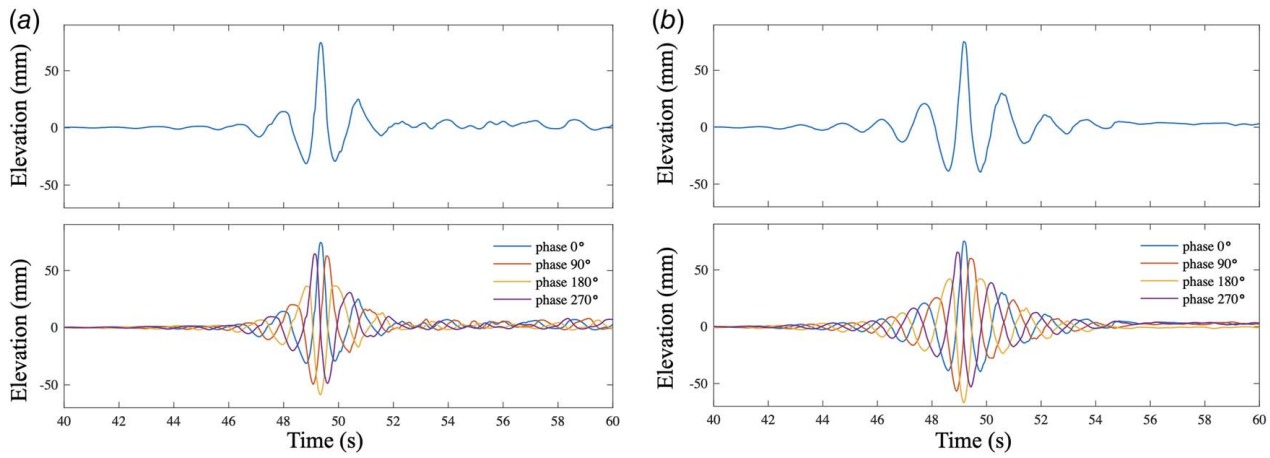
Fig. 8 Free-surface elevation of focused waves and its other three 90 deg-, 180 deg-, and 270 deg-shifted equivalents at the focus point in time histories for different wave spreading cases. (a) Bidirectional waves, $kR = 0.35$, $kA = 0.21$, $\theta = 40$ deg and (b) multidirectional waves, $kR = 0.35$, $kA = 0.23$, $\sigma = 30$ deg.
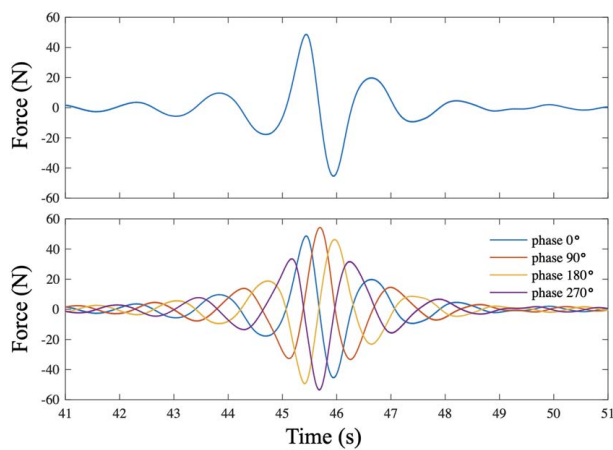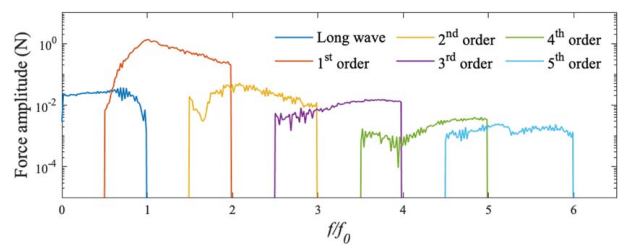

Fig. 9 Time histories of total inline wave forces on cylinder interacting with bidirectional waves shown in Fig. 8(a)
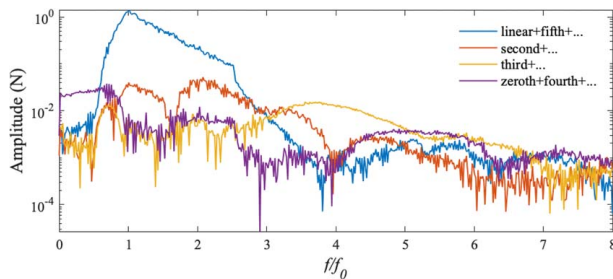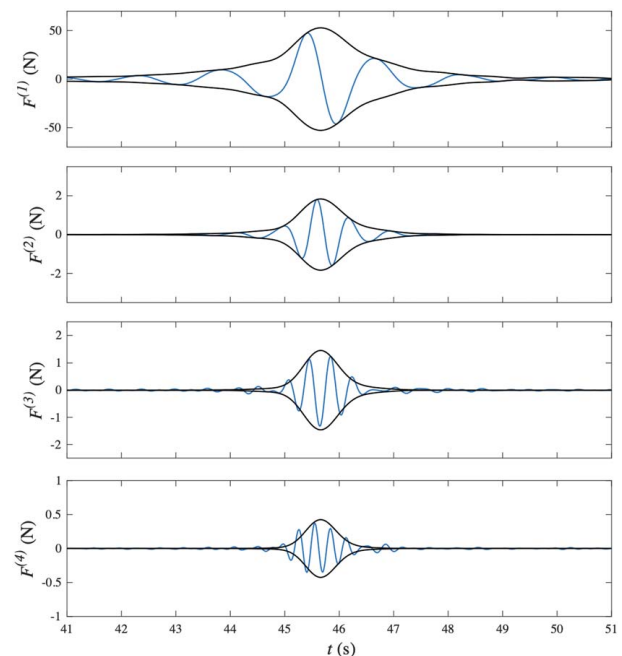

Fig. 10 Force amplitude spectrum of linear combinations from Eq. (1) for separated harmonic inline force components in bidirectional waves in Fig. 9

Fig. 11 Extracted force amplitude spectra for individual harmonics from the linear combinations in Fig. 10

Fig. 12 Time histories of extracted individual harmonic forces from the 0 deg phase total inline bidirectional force in Fig. 9. $F^{(n)}$ refers to the nth-order harmonic force.

this phase alignment, where the 90 deg, 180 deg, and 270 deg phase shifts correctly correspond to the 0 deg phase waves, which is crucial for the extraction of force harmonics using the four-phase method, has been clearly confirmed. This underscores the requirement for accurate timing and phasing of experimental data using the four-phase method.

3.2 Extraction of Individual Wave Force Harmonic.
The two example waves discussed in Sec. 3.1 are utilized for interaction with the cylinder, following the verification of the feasibility of
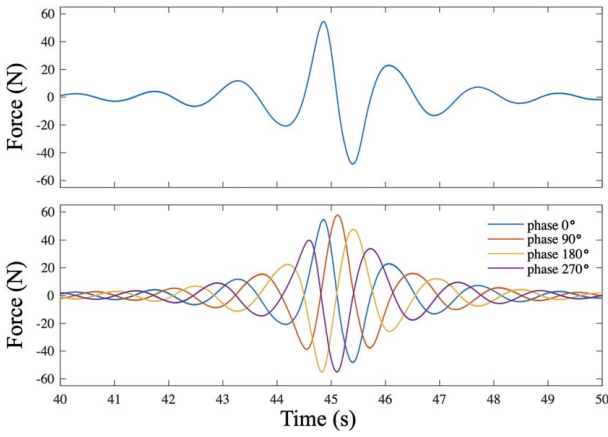
four-phase wave generation. Figure 9 displays the total force exerted on the cylinder by the four bidirectional wave phases shown in Fig. 8(a). The force amplitude spectra shown in Fig. 10 illustrate the combinations of wave force components calculated
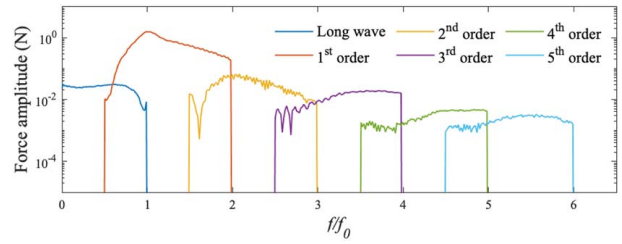
Fig. 13 Time histories of total inline wave forces on cylinder interacting with multidirectional waves shown in Fig. 8(*b*)
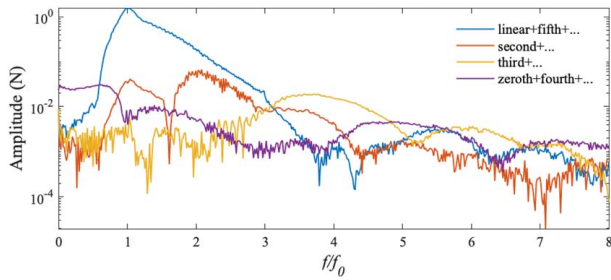

Fig. 14 Force amplitude spectrum of linear combinations from Eq. (1) for separated harmonic inline force components in multidirectional waves in Fig. 13

using Eq. (1). After applying the four-phase method equations, the linear and fifth-order harmonics are grouped within the same amplitude spectrum. This grouping ensures that the linear components are clearly separated from their neighboring harmonics, such as the zeroth (long wave component) and third-order harmonics, resulting in clean separation. Similarly, the second-, third-, and fourth-order harmonics are successfully isolated into other individual force amplitude spectra, as shown in Fig. 10. In Fig. 11, building on the results from Fig. 10, each individual harmonic spectrum is successfully extracted. This is achieved by retaining the values around


Fig. 15 Extracted force amplitude spectra for individual harmonics from the linear combinations in Fig. 14
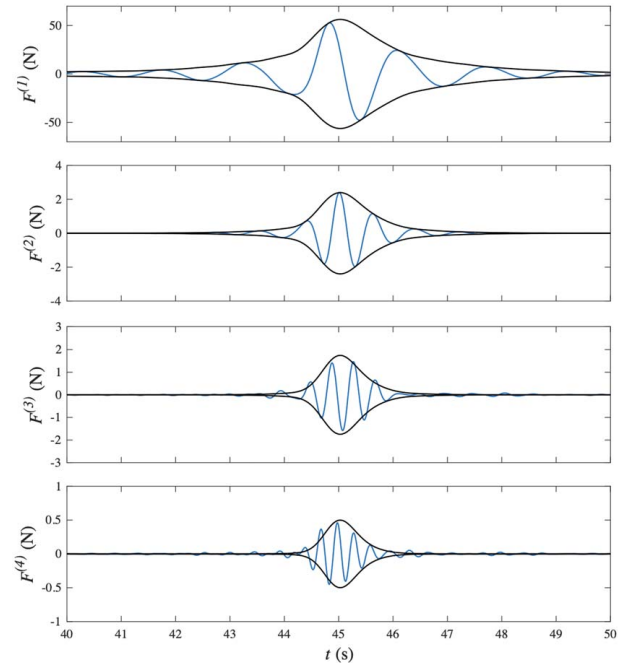
Fig. 16 Time histories of extracted individual harmonic forces from the 0 deg phase total inline multidirectional force in Fig. 13

the specific harmonic frequencies while setting all other values to zero outside the harmonic regions. By applying the inverse fast Fourier transform to each individual harmonic spectrum from Fig. 11, the time histories of the individual harmonics of the
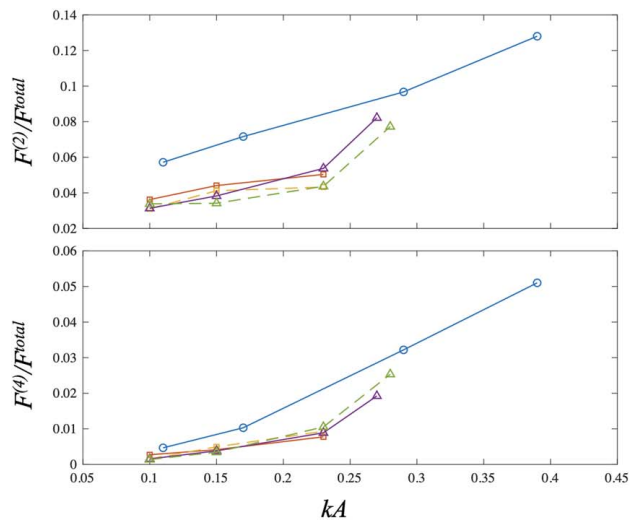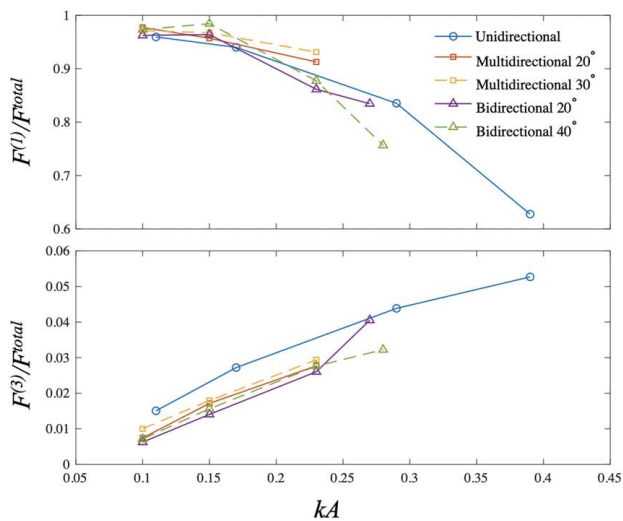
Fig. 17 Contribution of each harmonic force to total inline wave force as a function of *kA* with *kR* = 0.25 and *kd* = 1.40 in various wave spreading regimes. *F*(*n*)/*F*total represents the contributions of *n*th-order harmonics to the total force.

inline wave force are reconstructed, as shown in Fig. 12. These plots include the linear, second, third, fourth, and fifth sum harmonics, respectively. To display the distribution of wave forces, the individual harmonics are enveloped, a method that will be applied in Sec. 4 to assess the contributions of wave force components. The linear force envelope is obtained by applying the Hilbert transform. Envelopes of the nth-order harmonics (above the second order) are generated by elevating the linear envelope to the nth power and are displayed on the top of the corresponding harmonic components in Fig. 12. These are scaled using a least-squares method to match the size of the maximum measured nth-order harmonics. The wave conditions from Fig. 8(b) for the multidirectional wave case are also applied to the cylinder. The results in Figs. 13–16 show very similar outcomes to the bidirectional wave case.

The higher-order harmonics in Figs. 12 and 16 are generally encompassed by the envelopes derived from linear force envelopes. This relationship between higher-order harmonics and linear force is consistent with previous investigations of unidirectional waves in Ref. [1]. The extraction results prove the effectiveness of the four-phase method, even with bidirectional and multidirectional waves.

4 Contributions of Wave Force Harmonics

By utilizing the method outlined in Sec. 3, we have obtained each individual harmonic in time histories. The envelopes of force harmonics are employed to represent the distribution of wave forces. Figure 17 illustrates one group of test cases from our experiments, characterized by a peak wave period of 1.51 s, a peak wave number (k) of 2.00 m^{-1}, and a water depth of 0.7 m. The wave amplitude (A) refers to the main crest amplitude measured at the focus point in the empty tank. To prevent wave breaking prior to the focus point, kA is constrained to the largest amplitude achievable without wave breaking in front of the cylinder. Different wave spreading conditions may lead to varying nonlinear evolution within the wave tank, resulting in different maximum achievable kA values, as demonstrated in Fig. 17. The achievable kA in the tank reaches 0.39 for unidirectional waves, 0.28 for bidirectional waves, and 0.23 for multidirectional waves in our wave tank.

In Fig. 17, $F^{(n)}/F^{\text{total}}$ indicates the contributions of nth-order harmonics to the total force. Analyzing the contributions of the linear force ($F^{(1)}/F^{\text{total}}$), it is evident that unidirectional waves with $kA = 0.39$ exhibit the smallest distribution of linear components. This inversely reflects the significant nonlinearities in the inline wave forces on the cylinder, accounting for about 40% of the total force. In contrast, the multidirectional and bidirectional waves demonstrate lower nonlinearities, with the largest values being 10% and 25%, respectively.

Concerning the general tendency, the contributions of the second, third, and fourth harmonics in unidirectional waves are consistently more significant than in the other spread sea cases for the same kA. The root-mean-square angle of the multidirectional waves, varying from 20 deg to 30 deg, and the angle between crossing waves in bidirectional waves, varying from 20 deg to 40 deg, have a minor impact on the variation in contributions of each harmonic. However, some outliers are observed when bidirectional waves approach the breaking limit; the contribution of linear components decreases more rapidly than in unidirectional wave cases. In this context, given the relatively minor contributions from the second- to fourth-order harmonics, we anticipate a marked increase in the contributions of higher-order harmonics (beyond the fourth order) under these near-breaking conditions.

Overall, in terms of the contributions of individual harmonics, the nonlinearities of unidirectional waves stand out as the most pronounced among the different spreading conditions.

5 Conclusion

This research extends the investigation into higher-order harmonic forces, moving beyond unidirectional waves to encompass various wave spreading conditions. Through an exploration of wave patterns, this study confirms that forces under directionally spread wave conditions follow the Stoke-type harmonic series. Additionally, the research has demonstrated the versatility and effectiveness of the four-phase inversion method in diverse wave-spreading scenarios.

By adapting the four-phase inversion method, initially validated for unidirectional waves, to both bidirectional and multidirectional contexts, we successfully separated and analyzed individual harmonic components from the total wave forces. This capability enhances the understanding of nonlinear wave loads in realistic ocean conditions, where directionally spread waves are more prevalent than unidirectional ones.

A significant finding of the research is the pronounced nonlinearity observed in unidirectional waves, which stands out when compared to bidirectional and multidirectional wave cases. The contributions of higher-order harmonic forces in these different wave-spreading conditions were quantitatively assessed, offering valuable insights into the complex dynamics of wave–structure interactions.

Overall, this study provides a robust methodology for analyzing nonlinear wave forces in diverse and realistic wave environments, contributing to a deeper understanding of wave-induced loads on offshore structures. This advancement has important implications for the design and safety of offshore wind turbines and other marine structures exposed to harsh environmental conditions.

Conflict of Interest

There are no conflicts of interest.

Data Availability Statement

The datasets generated and supporting the findings of this article are obtainable from the corresponding author upon reasonable request.

References

[1] Chen, L. F., Zang, J., Taylor, P. H., Sun, L., Morgan, G. C. J., Grice, J., Orszaghova, J., and Tello Ruiz, M., 2018, "An Experimental Decomposition of Nonlinear Forces on a Surface-Piercing Column: Stokes-Type Expansions of the Force Harmonics," J. Fluid Mech., 848, pp. 42–77.
[2] Molin, B., 1979, "Second-Order Diffraction Loads Upon Three-Dimensional Bodies," Appl. Ocean Res., 1(4), pp. 197–202.
[3] Eatock Taylor, R., and Hung, S. M., 1987, "Second Order Diffraction Forces on a Vertical Cylinder in Regular Waves," Appl. Ocean Res., 9(1), pp. 19–30.
[4] Newman, J. N., 1996, Nonlinear Scattering of Long Waves by a Vertical Cylinder, Springer, Dordrecht, Netherlands, pp. 91–102.
[5] Faltinsen, O. M., Newman, J. N., and Vinje, T., 1995, "Nonlinear Wave Loads on a Slender Vertical Cylinder," J. Fluid Mech., 289, pp. 179–198.
[6] Huseby, M., and Grue, J., 2000, "An Experimental Investigation of Higher-Harmonic Wave Forces on a Vertical Cylinder," J. Fluid Mech., 414, pp. 75–103.
[7] Chaplin, J. R., Rainey, R. C. T., and Yemm, R. W., 1997, "Ringing of a Vertical Cylinder in Waves," J. Fluid Mech., 350, pp. 119–147.
[8] Grue, J., and Huseby, M., 2002, "Higher Harmonic Wave Forces and Ringing of Vertical Cylinders," Appl. Ocean Res., 24(4), pp. 203–214.

[9] Riise, B. H., Grue, J., Jensen, A., and Johannessen, T. B., 2018, "High Frequency Resonant Response of a Monopile in Irregular Deep Water Waves," J. Fluid Mech., **853**, pp. 564–586.

[10] Mj, D., McAllister, M. L., Bredmose, H., Adcock, T. A. A., and Taylor, P. H., 2023, "Harmonic Structure of Wave Loads on a Surface Piercing Column in Directionally Spread and Unidirectional Random Seas," J. Ocean Eng. Mar. Energy, **9**(3), pp. 415–433.

[11] Fitzgerald, C. J., Taylor, P. H., Eatock Taylor, R., Grice, J., and Zang, J., 2014, "Phase Manipulation and the Harmonic Components of Ringing Forces on a Surface-Piercing Column," Proc. R. Soc. A: Math. Phys. Eng. Sci., **470**(2168), p. 20130847.

[12] Tang, T., Ding, H., Dai, S., Chen, X., Taylor, P., Zang, J., and Adcock, T. A. A., 2024, "Data Informed Model Test Design With Machine Learning—An Example in Nonlinear Wave Load on a Vertical Cylinder," ASME J. Offshore Mech. Arct. Eng., **146**(2), p. 021204.

[13] Hersbach, H., Bell, B., Berrisford, P., Hirahara, S., Horányi, A., Muñoz-Sabater, J., Nicolas, J., et al., 2020, "The ERA5 Global Reanalysis," Q. J. R. Metereol. Soc., **146**(730), pp. 1999–2049.

[14] Li, J., Zhang, H., Liu, S., Fan, Y., and Zang, J., 2022, "Experimental Investigations of Secondary Load Cycle Formation in Wave Force on a Circular Cylinder Under Steep Regular Waves," Ocean Eng., **253**, p. 111265.

[15] Lindgren, G., 1970, "Some Properties of a Normal Process Near a Local Maximum," Ann. Math. Stat., **41**(6), pp. 1870–1883.

[16] Boccotti, P., 1983, "Some New Results on Statistical Properties of Wind Waves," Appl. Ocean Res., **5**(3), pp. 134–140.

[17] Hasselmann, K., Olbers, D., et al., 1973, "Measurements of Wind-Wave Growth and Swell Decay During the Joint North Sea Wave Project (JONSWAP)," Ergänzung zur Deut. Hydrogr. Z. Reihe A, **12**(8), pp. 1–95.

[18] Lo, B. E., and Mei, C. C., 1985, "A Numerical Study of Water-Wave Modulation Based on a Higher-Order Nonlinear Schrodinger Equation," J. Fluid Mech., **150**, pp. 395–416.

[19] Baldock, T. E., Swan, C., and Taylor, P. H., 1996, "A Laboratory Study of Nonlinear Surface Waves on Water," Philos. Trans. R. Soc., A, **354**(1707), pp. 649–676.

[20] Longuet-Higgins, M. S., Cartwright, D. E., and Smith, N. D., 1963, "Observations of the Directional Spectrum of Sea Waves Using the Motions of Floating Buoy," Ocean Wave Spectra, Prentice-Hall Inc., Englewood Cliffs, NJ, pp. 111–136.

[21] Ji, X., Liu, S., Li, J., and Jia, W., 2015, "Experimental Investigation of the Interaction of Multidirectional Irregular Waves With a Large Cylinder," Ocean Eng., **93**, pp. 64–73.

[22] Ji, X., Liu, S., Bingham, H. B., and Li, J., 2015, "Multi-Directional Random Wave Interaction With an Array of Cylinders," Ocean Eng., **110**, pp. 62–77.

[23] Stokes, G. G., 1847, "On the Theory of Oscillatory Waves," Trans. Cambridge Philos. Soc., **8**, pp. 441–455.

[24] Zang, J., Gibson, R., Taylor, P. H., Eatock Taylor, R., and Swan, C., 2006, "Second Order Wave Diffraction Around a Fixed Ship-Shaped Body in Unidirectional Steep Waves," ASME J. Offshore Mech. Arct. Eng., **128**(2), pp. 89–99.

[25] Adcock, T. A. A., Feng, X., Tang, T., Van Den Bremer, T. S., Day, S., Dai, S., Li, Y., Lin, Z., Xu, W., and Taylor, P. H., 2019, "Application of Phase Decomposition to the Analysis of Random Time Series From Wave Basin Tests," Proc. Int. Conf. Offshore Mech. Arct. Eng., **9**, pp. 1–10.

[26] Tang, T., Ryan, G., Ding, H., Chen, X., Zang, J., Taylor, P. H., and Adcock, T. A. A., 2024, "A New Gaussian Process Based Model for Non-Linear Wave Loading on Vertical Cylinders," Coast. Eng., **188**, p. 104427.